Babes-Bolyai University
Faculty of Physics

Doctoral thesis summary

Antibody-targeted plasmonic nanoparticles for potential theranostic applications in Acute Lymphoblastic Leukemia

by
Andra-Sorina Tătar

Scientific Advisor
Prof. Dr. Simion Astilean

CLUJ-NAPOCA
2019

TABLE OF CONTENTS

Keywords: plasmonic nanoparticles, biofunctionalisation, specific interactions, multimodal imaging, theranostic agents, acute lymphoblastic leukemia

The rise of Nanomedicine as an emerging field that tackles a wide range of medical issues was possible due to the recent developments in nanotechnology. Thus, state-of-the-art nanomaterials can offer superior solutions when used in conjunction with conventional medicine. This thesis aims to develop a type of nanoparticle-based agent that is capable to track, image, and simultaneously damage Acute Lymphoblastic Leukemia (ALL) cells, whilst demonstrating biocompatibility toward healthy cells. Specifically, the developed theranostic nanoparticles are tracked intracellularly through multiple fast and non-invasive imaging techniques including Surface-enhanced Raman spectroscopy (SERS), Dark-Field microscopy, Fluorescence Lifetime Imaging (FLIM). The cytotoxic effect against the malignant cells was proved by Cell Counting and further investigated by Cell Cycle analysis by Flow Cytometry and MTS assay.

The thesis is structured in seven chapters. The **1ˢᵗ Chapter** is a comprehensive overview on the therapeutic approaches against ALL from conventional methods to nanomedicine. It contains a thorough description of the genetic basis of ALL, followed by a presentation of the conventional protocol typically employed in the medical centers for ALL patients. An overview of the immunological characteristics of the diseased cells transfers the reader toward the section focused on nanomedicine applications for ALL. After the principles and main advantages of nano-medicinal concepts are explained, a literature review of nanoparticle-based approaches used against ALL is presented, demarcated based on their composition into organic and inorganic nanoparticles. Following this is a discussion regarding the safety issues and challenges for clinical translation of anti-ALL nanomedicine.

The following chapters are focused on the experimental part of my work, each with a brief Introduction that covers the main aspects in consideration, Materials and Methods, and the Results and Discussions. Specifically, the **2ⁿᵈ Chapter** follows the synthesis steps that lead to the production of antibody-conjugated, polymer-coated, Raman-tagged nano-particles. We then discuss the size and shape tailoring of the nanoparticles, which is what confers them plasmonic responses in the near infra-red (NIR) domain, the electromagnetic range most suitable for medical applications, where tissues are characterized by a minimum absorption. The particles are further tagged with Raman reporters that will be employed for intracellular nanoparticle tracking through SERS, and polymer molecules are grafted at their surface to increase stability and ensure bio-compatibility. The final bioconjugation step is the attachment of antibody molecules, which grant the nanosystem specificity of interaction with the targeted ALL cell lines. In this work, two

classes of nanoparticles were developed. First, the tailoring of star-like particles allowed the creation of nanostars and nanourchins, respectively, among which the nanourchins were selected for further experiments, while the second class of particles employed in following steps are hollow nanospheres.

The **3rd Chapter** explores the potential of the developed nanourchins and hollow nanospheres for imaging *via* multiple fast, non-invasive, and non-destructive spectroscopic techniques. Thus, Dark-Field microscopy offers images of the antibody-targeted nano-particles internalised by ALL cells based on their high scattering properties. Additionally, confocal Raman microscopy allows intracellular particle tracking based on the molecular signature of the loaded Raman reporter, whose signal is highly enhanced through the SERS effect. Thirdly, FLIM is an additional type of imaging technique able to discern the nanoparticles within the cellular microenvironment based on the difference in fluorescence lifetime values. All in all, the multimodal imaging character of the developed nanoparticles, combined with their antibody-based specificity of interaction highlights their potential as targeting and diagnosis tools which could be employed for an early detection of the disease, and thus increasing the survival chances of the patients.

The **4th Chapter**, based on Transmission Electron Microscopy (TEM), offers an in-depth high resolution validation of the interaction of antibody-targeted nanourchins and hollow nanospheres with the target cells. Using multiple control samples such as non-targeted nanoparticles, non-target cells, and competitive binding assays, we demonstrate the high specificity of the antibody-targeted nanoparticles for the antigen-expressing ALL cells.

The **5th Chapter** is focused on the cytotoxic effect of antibody-targeted nanourchins and demonstrates their therapeutic potential. Relevant control samples such as non-targeted nanourchins and free antibody molecules are tested and the results indicate an increased effect of the nano-system components when used in combination. Additional Cell Cycle analysis by Flow Cytometry and MTS assays are performed to bring more clarity into the mechanisms of action of the antibody-targeted nanourchins onto the ALL cell line, revealing a high level of oxidative stress as a major potential path toward the onset of late apoptosis.

All in all, this work proves the potential of the developed antibody-targeted noble-metal nanoparticles to function as theranostic agents in the fight against Acute Lymphoblastic Leukemia, and thus, in **Chapter 6** I will reiterate the main conclusions of this work.

1. Overview of the therapeutic approaches against Acute Lymphoblastic Leukemia: from conventional methods to nanomedicine

1.1 Basics of Acute Lymphoblastic Leukemia

Acute lymphoblastic leukemia (ALL) is a malignancy characterised by the uncontrolled proliferation of lymphoid cells leading to an overpopulation of the blood by lymphoblastst in the detriment of normal blood cells. Although significant improvements in pediatric ALL survival rates were achieved in the last decades (going from 57% to 92% [1]) through improvements in risk stratification, supportive care, and diagnosis precision for personalised chemotherapy [2,3], remission in adult ALL cases only reaches 30 to 40%, most probably influenced by additional implications of adult comorbidities and youth-related favouring circumstances.

ALL disease classification is based on multiple cellular and sub-cellular features, such as cell morphology, genetic and cytogenetic features and immunophenotype. Non-random gross chromosomal alterations are identified in most ALL cases, generally in the form of aneuploidies and paired translocations of chromosome fragments, combined with submicroscopic genetic alterations (indels and SNPs) in key oncogenes. The distribution of ALL subtypes and mutations varies between pediatric and adult cases (Figure 1.1), also inducing the different disease outcomes for each age-group.

Throughout the years, improvement in ALL therapy and survival rates was achieved by conventional treatment intensification and the use of conventional treatments in combinatorial manners [4]. The most recent research is now focusing on developing new molecular approaches, and nanobiotechnology through the use of nanoscale-devices and nanomaterials, currently making strides in the applicative area of cancer treatment for diagnosis, drug delivery, and therapeutics [5,6].

1.2 Immunological approach

Drugs based on monoclonal antibodies represent a new therapeutic option for the clinical management of ALL, as the leukemia cells almost always present an overexpression of various surface antigens that can be targeted with specific humanized monoclonal antibodies (mAbs). An ideal target molecule has a high expression profile on the malignant cell surface and is not

present on healthy cells, thus increasing the selectivity of the treatment and reducing off-tumor toxicity. Surface proteins with potential for ALL targeting are CD3 and CD7 for T-cell ALL, while B-ALL is best targeted *via* the CD19, CD20, or CD22 proteins. The main advantage of immunologically based treatments is the targeted localisation of the cytotoxic substance, leading to a lower overall dose of toxic agent needed and reduced side-effects. Nevertheless, negative symptoms can still occur, mostly as a result of hyperexcitation of the immune system, with common symptoms like fever, weakness, headaches, nausea.
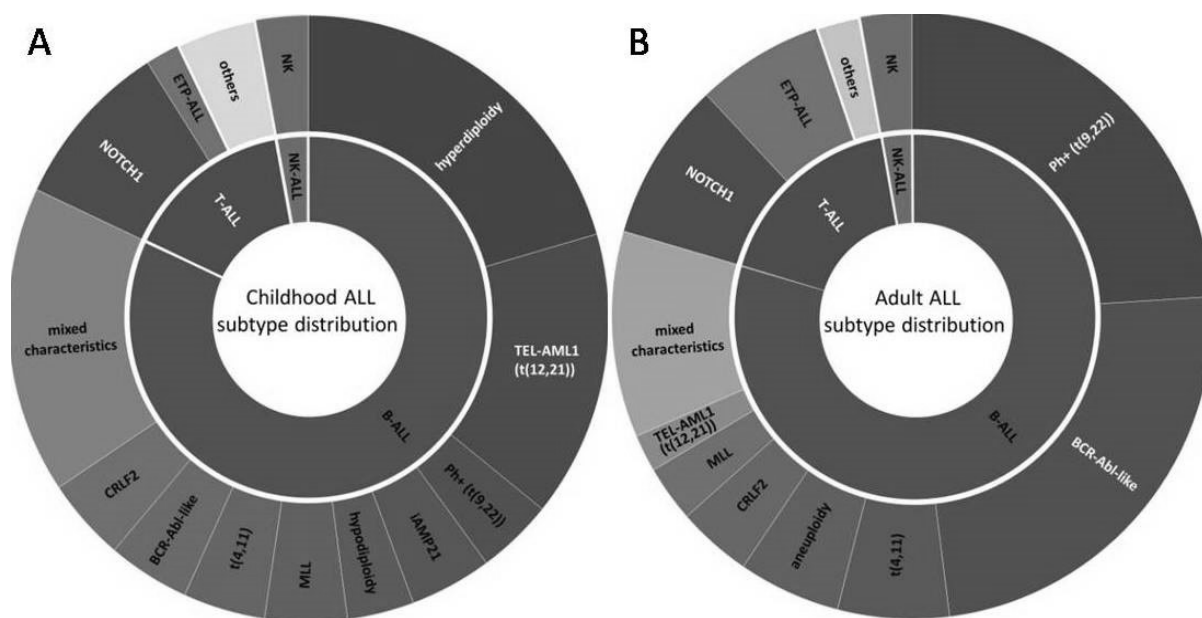
Figure 1.1 Relative distribution of ALL in (A) children and (B) adults, with subtypes represented for each cell-type.

1.3 Nanomedicine for ALL detection and treatment

1.3.1 Nanoparticle-based strategies for improved biomedical applications

Nanomedicine encompasses distinct application areas that use carefully tuned and constructed nano-sized material systems (that are on the size-scale of biological structures), such as *in vivo* imaging and *in vitro* diagnosis, drug delivery and targeted therapy, and extends to the use of biomaterials as active implants [7]. Organic nano-materials offer advantages based on the mimetics of natural organic structures, and can come in many variations of polymers and lipids. These properties can be helpful to avoid bio-fouling of the nanoparticle, to prolong circulation time, to evade the body immune system, and many more. They are also quite flexible and can

pass through different barriers, junctions, or cellular membranes. Inorganic nanoparticles, on the other hand, such as magnetic nanoparticles, noble metal nanoparticles, and others have extraordinary physical properties that can be manipulated by tuning their composition, size or shape. New imaging possibilities arise from the combination of the optical properties of inorganic nanoparticles with imaging techniques, while the therapeutic aspect is also enriched in many ways, such as by hyperthermia and controlled drug release strategies. Hybrid nanoparticles offer the possibility for simultaneous cancer detection and therapy (theranostics) or the combination of two or more different therapeutic strategies (drug delivery, gene delivery, hyperthermia, photodynamic therapy, sequential delivery of therapeutics etc.), which can considerably increase the effectiveness of the treatment [8].

Improved aiming of the malignant cells or tissues by using nanostructured agents is possible due their particular targeting properties. Nano-sized materials are *passively targeting* tumor tissues, through a process known as enhanced permeability and retention (EPR) effect. The EPR takes place due to a reduced lymphatic drainage in the tumoral mass and a poorly formed fenestrated endothelium in the tumoral neo-vascularisation. An improved form of nanoparticle targeting is *active targeting*, which refers to the conjugation of molecular ligands on the particle surface, preferably on top of the stealth layer, aimed to recognize certain over-expressed markers on the cancer cells. Efficient biological targeting moieties can vary from antibodies and their constitutive fragments, to various other proteins, peptides and also aptamers [9]. An additional approach to targeting is based on the physical characteristics of the nanoparticles, such as magnetic field gradient guiding of magnetic nanoparticles towards the biological targets.

A high proportion of the nanoparticle formulations contain a payload that is supposed to be released at the cancer site to impart therapeutic or imaging applications. Payload release can be triggered in a somewhat *passive* way by specific microenvironmental conditions created at the targeted cancer site, such as the slighlty increased physiological temperature due to the higher metabolic rates, and local variations in pH or other enzymatic activities. More *active* ways of payload release can be manipulated by external stimuli, such as ultrasounds or magnetic and electric fields, which can lead to very effective hyperthermic effects if combined with magnetic or noble-metal nanoparticles.

1.3.2 Organic nanoparticles for ALL detection and treatment

The nature of organic nanoparticles such as liposomes and polymeric nanoparticles more closely resembles biological structures making them weakly immunogenic, biocompatible, and biodegradable. The small size, porous structure, and chemical composition allow a high loading capacity for both hydrophilic and hydrophobic molecules. A multitude of functional groups at the particle surface allows easy functionalization with specific targeting elements such as antibodies, peptides, and other organic molecules for lock-and-key recognition of cancer-cell specific biomarkers.

1.3.3 Inorganic nanoparticles for ALL detection and treatment

Inorganic nanoparticles can exhibit more diverse and distinct size and composition-dependent physical properties which render them suitable for biomedical applications such as cell imaging and molecular detection. They are usually combined in hybrid forms, as the organic component offers complementary properties such as solubility in physiological media, active sites for bio-conjugation, biocompatibility etc. Graphene based nano-materials, when used in the oxidized form of graphene oxide, are adequate for biomedical applications due to the amphiphilic nature and many available functional groups used for applications such as biosensoristics, bioimaging or drug delivery.

Noble metal nanoparticles are highly valuable due to their unique optical properties such as the surface plasmon resonance (SPR), a phenomenon of resonant electron oscillations that leads to the appearance of a high electric field in the particle close vicinity. These particles can strongly absorb and scatter light. Thus, sensitive detection can lead to a more prompt treatment and higher chances of recovery, while through the use of Surface-Enhanced Raman Scattering (SERS), the probing of cells and tissues at the molecular level and the biomedical imaging using tagged nanoparticles as contrasting agents are made possible. NIR responsive plasmonic nanoparticles are efficient light-to-heat converters that can be used to achieve hyperthermia or controlled payload release inside living cells, and their high surface-to-volume ratio allows a high loading of payload molecules for various applications.

Bio-targeting moieties bound to the particles can infer specificity of interaction towards the target cells, and adding Raman reporters or fluorescent molecules to nanostructures allows their imaging and detection using fast and non-invasive techniques. Based on the unique and

interesting properties of nanoparticles, their use in the near future anti-cancer diagnosis, imaging and therapy shows promising prospects.

1.4 Safety issues and challenges for clinical translation of nanomedicine

The risks emerging from the size scale of the nanoparticles concerns effects ranging from the sub-cellular and cellular level, to organ specific accumulations, and to whole body influences. At the nuclear level, GNP can fit along the phosphate backbone of the DNA macromolecule, thus affecting biological processes such as transcription, replication, protein expression, or even inducing cell apoptosis or necrosis. Cellular integrity, motility, proliferation and adhesion were shown to be impaired *in vitro* due to high concentrations of NP, along with a deterioration of the actin filaments of the cytoskeleton [10]. Oxidative stress was pointed out [11]. Particles with diameters over 50 nm gathered significantly in the liver and spleen and remained there for 3 to 4 months, while 10 nm particles congregated in organs such as kidneys, testes, thymus, heart, lungs, brain. Nevertheless, a large number of studies did not point out any toxicity of the NP, as they maintained concentrations lower than 10^{12} particles/ml [12].

RESEARCH RESULTS AND DISCUSSIONS

2. Plasmonic nanoparticles: synthesis tailoring, biofunctionalisation, characterization

2.1 Gold nanostars

Nanostar size and shape variation was obtained by tuning the synthesis protocol [13], using 3 different $AgNO_3$ concentrations which are identified as samples A (0.5 mM), B (1 mM), and C (2 mM) - Figure 2.1. The UV-Vis extinction spectra of the particles span the electromagnetic spectrum from red to near-infra-red, based on the Surface Plasmon Resonance (SPR) shifts induced by the lengthening of the particle spikes. Optical characterization data, TEM-based measurements characterizing the particle morphology, hydrodynamic diameter informations obtained by Dinamic Light Scattering (DLS), and the Zeta-potential of the particles are presented in Table 2.1. The highest $AgNO_3$ concentrations aid the growth of long protuberances, and even branching, while the lowest $AgNO_3$ concentration leads to more gold deposition on the particle core and little spike growth.
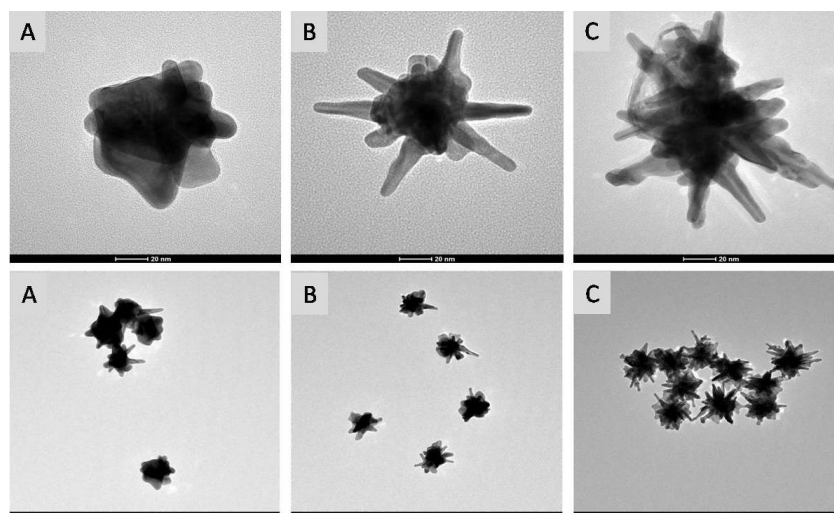
Figure 2.1 TEM micrographs of samples A (A), B (B), and C (C). Scale bars are 20 nm in top row, and 100 nm in bottom row.

For the exploration of the nanostar SERS properties, we tested the Raman reporters NB and pATP, for which the potential mechanisms of interaction with the gold surface are adsorption at the metal surface through delocalized pi-electrons and covalent thiol S-Au conjugation, respectively. The obtained SERS signal intensity values are presented in Table 2.1. Enhancement for NB proved to be the most efficient among our tests, with SERS signal as high as 10^5 counts for the 595 cm^{-1} phenoxazine ring stretching vibration band, while the pATP SERS signal of the 1075 cm^{-1} C-C and C-S stretching vibration band reached around 10^3 counts. SPR red-shifts of a few nanometers confirm both the reporters' presence at the particle surface.

Table 2.1 Characterisation data of samples A, B and C.

	Sample:	A	B	C
UV-Vis	SPR position (nm)	642	690	792
	FWHM of SPR (nm)	127	161	254
TEM	core diameter (nm)	69.6 ± 7.2	49.3 ± 6.2	55 ± 13.1
	spike length (nm)	9.5 ± 4	21 ± 5.5	30.3 ± 7
	spike number (in 2D projection)	4 ± 1	11 ± 3	16 ± 6
	nanostar size (nm)	88.6 ± 8.2	91.3 ± 10.4	115.6 ± 21.7
DLS	hydrodynamic diameter (nm)	101.3	98.3	118
	Zeta-potential (mV)	-37	-33	-37
SERS intensity	Nile Blue (kcounts)	17	100	23
	pATP (kcounts)	1.7	1.8	1

After PEG-ylation of the Raman-tagged particles, the SERS signal was found to increase slightly, despite a washing step necessary in the process. This is explained by the confinement of reporter molecules in the close vicinity of the particle surface, as they are caught between the PEG chains in a process known as steric shielding.

2.2 Gold Nanourchins

Additional optimization of the nanostar synthesis protocol allowed us to obtain a more red-shifted SPR band of the particles (at 900 nm), with longer spikes (due to higher $AgNO_3$ concentration) and less branching (increased reducing agent concentration), resembling the sea-urchins (Figure 2.2). TEM-based measurements showed an average NP core diameter of 101±12 nm, average branch length of 31.9±12.9 nm, and an average 2D projection of the branch number per NP of 16.8±3.5. Particle Raman tagging resulted in a NB SERS signal intensity of 35 kcounts, for the same measurement settings as those used for nanostars. The following conjugation steps were tracked and characterized to ensure correct bio-functionalisation, and the data is shown in Table2.2. Particle stability was monitored over time, and the polymer coating seems to offer sufficient steric stability, even at 6 months after biofunctionalisation.
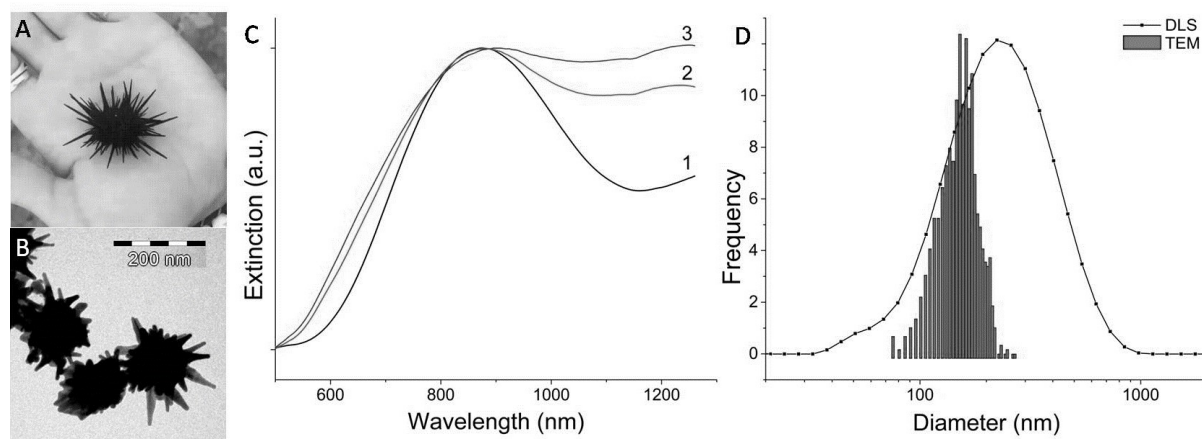

Figure 2.2 A: photography of a sea urchin; B: TEM micrograph of the GNU sample; C: extinction spectra of newly synthesized GNU (1), PEG-NB-GNU (2), and antiCD19-PEG-NB-GNU (3); D: size distribution of GNU based on DLS measurements and TEM micrograph analysis.

Table2.2. Zeta-potential values, NB SERS signal intensity, hydrodynamic diameters and PDIs characteristic for each step during the functionalisation protocol of the GNUs.

	Zeta-potential (mV)	SERS intensity* (kcounts)	Hydrodynamic diameter (nm)	PDI
GNU	-39.7±0.7	-	201.5±1.5	0.28±0.03
PEG-NB-GNU	-9.7±0.4	25.5	310.4±0.6	0.3±0.004
antiCD19-PEG-NB-GNU	-10.6±0.7	17.8	372.8±11.1	0.39±0.07

*SERS intensity measured for the NB specific 595 cm^{-1} phenoxazine ring stretching vibration

The concentration of antibody that was bound to the GNU after conjugation was assessed indirectly from the difference between the total added antibody and the unbound molecules, which were quantified based on a calibration curve of the fluorescence signal of FITC molecules (excitation at 495 nm, emission at 520 nm) that are conjugated to the antibody molecules by the producer. Our calculations show a final antiCD19 concentration of 5.97 µg/ml attached to the surface of the PEG-NB-GNU.

2.3 Hollow Nanospheres

In order to obtain a hollow spherical shape, the galvanic replacement method is used, where the material in spherical silver nano-seeds is oxidized by gold, which has a higher reduction potential: for every Au^{3+} ion in the boiling solution that is reduced to Au^0, 3 Ag^0 are oxidized and dissolved as Ag^+ ions. By controlled variation of the shape and size of the sacrificial template and the porosity and thickness of the shell-like structure, one can fine-tune the plasmon resonance of the particles [14]. Herein, hollow nanoparticles with a 720 nm response (Figure 2.3A, spectrum 2) were chosen for further experiments, based on their superior SERS effect and improved structural stability [14]. NB tagging was done using a Reporter concentration that results in a maximum SERS signal intensity. The ensuing bio-functionalisation steps were tracked and characterized and the data is shown in Table 2.3 and Figure 2.3A, spectra 3 and 4.
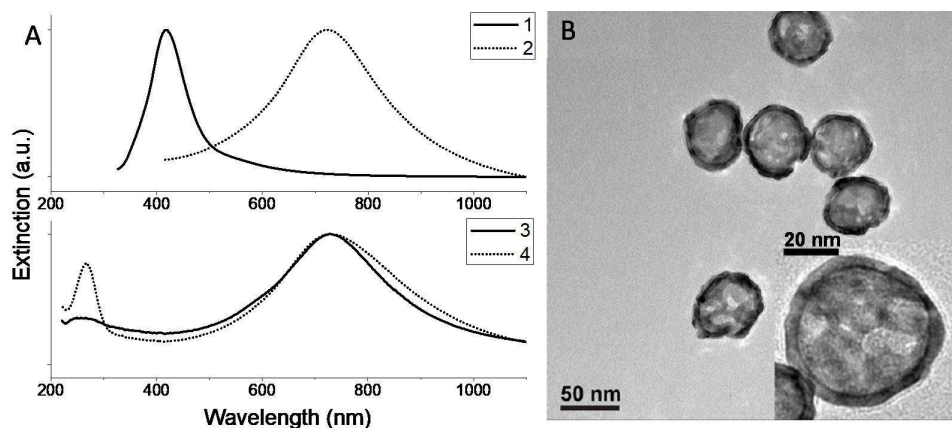

Figure 2.3 A: Extinction spectra of silver sacrificial templates (1), HNS (2), PEG-NB-HNS (3), antiCD19-PEG-NB-HNS (4); B: TEM micrographs of HNS used in this work.

The concentration of antibody that was bound to the HNS after conjugation was assessed using a similar protocol as in the case of GNU. Our calculations show a final antiCD19 concentration of 5.7 µg/ml attached to the surface of the PEG-NB-HNS.

Table 2.3 Zeta-potential values, NB SERS signal intensity, hydrodynamic diameters and PDIs characteristic for the Ag seeds and the ensuing functionalisation steps of the NHS

	Zeta-potential (mV)	SERS intensity* (kcounts)	Hydrodynamic diameter (nm)	PDI
Ag seeds		-	69.3 ±0.6	0.59
PEG-NB-HNS	-16	9	82.06±0.8	0.18
antiCD19-PEG-NB-HNS	-24.7	8	91.13±1.52	0.24

*SERS intensity of NB specific 595 cm^{-1} phenoxazine ring stretching vibration

3. Intracellular spectroscopic imaging of nanoparticles

3.1 Intracellular tracking of Gold Nanourchins

3.1.1 Dark-Field microscopy

The antiCD19-PEG-NB-GNUs have a high scattering cross-section value that allows imaging by dark-field microscopy and can be seen as yellow-orange luminous spots in the peripheral region of the cell cytoplasm or on the membrane of cellular extensions (Figure 3.1A, B). As a confocal technique, dark-field imaging confirms the intracellular distribution of the particles at different depths inside the cells. The results corroborate with those obtained with the other techniques (SERS, TPE-FLIM and TEM) in regard to the specificity of the CD19-based interaction, with a ratio of the number of counted bright-spots per cell of 5:1 for the antiCD19-PEG-NB-GNU *versus* the PEG-NB-GNU incubated cells
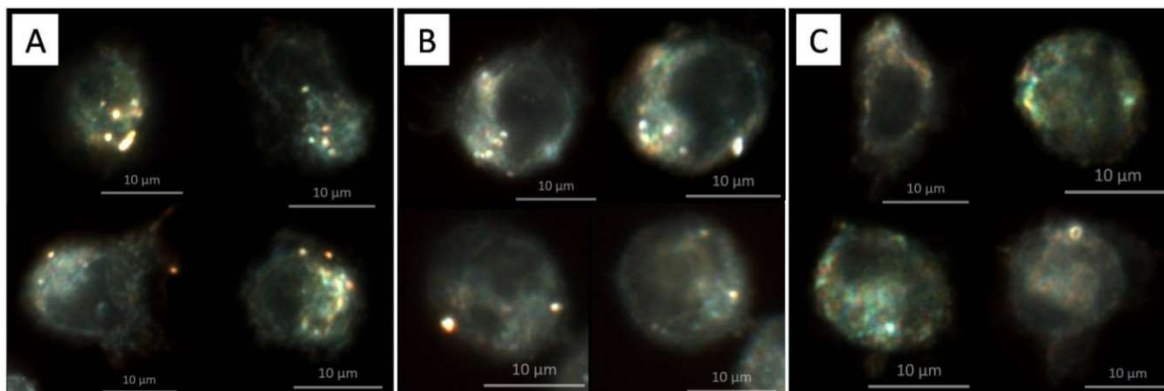

Figure 3.1 Dark-field images of cells treated with antiCD19-PEG-NB-GNU (A), PEG-NB-GNU (B) and untreated CCRF-SB cells (C).

3.1.2 Confocal Raman microscopy

Raman maps of cells incubated in the presence of nanoparticles, and of control cells without nanoparticles were built based on the univariate spectral analysis of the data (Figure 3.2). The antiCD19-PEG-NB-GNU incubated sample shows the particle presence through the NB

signal at 595 cm^{-1} (cyan pixels), and the red pixels represent the 1450 cm^{-1} band of the CH$_2$ and CH$_3$ deformation bands in proteins and lipids. The intensity of this band is increased by 15x fold compared to the organic ordinary Raman signal of the control sample (D). This affirms the presence of the SERS active nanoparticles, as they enhance not only the NB signal, but also that of organic molecules located in their close vicinity. Tentative band assignments based on the literature [15] are listed in Table 3.1.
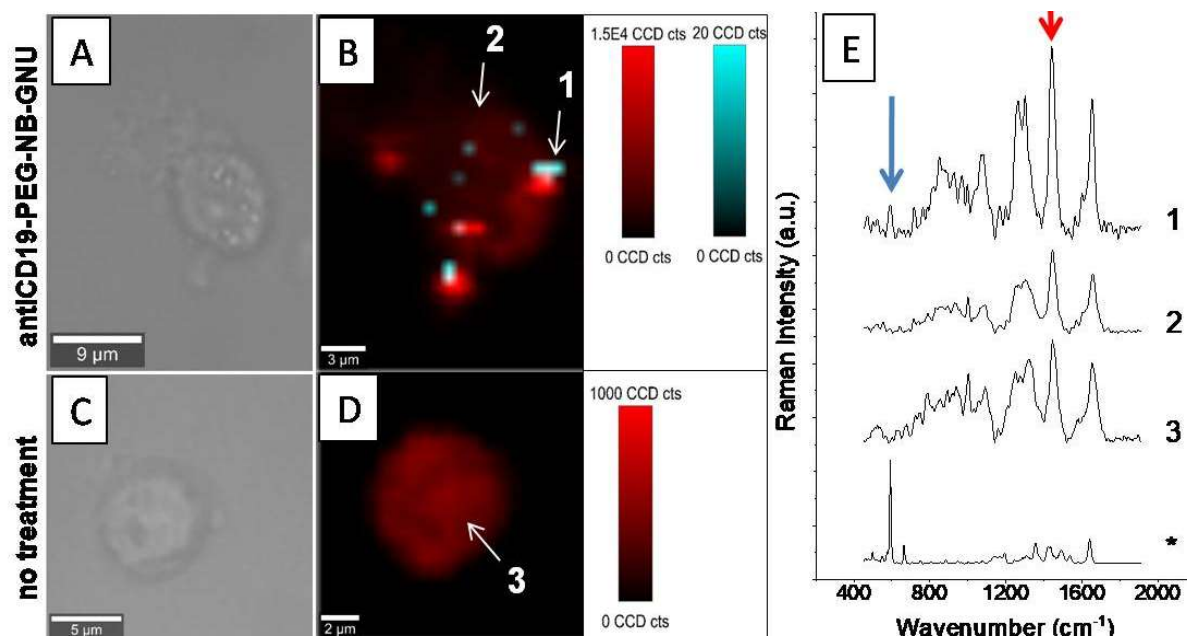

Figure 3.2 Bright-field optical images (A, C) and spectral maps of antiCD19-PEG-NB-GNU treated (B), and untreated CCRF-SB cells (D), constructed to highlight organic signal intensity (red) and the NB SERS signal (cyan). (E): Raman and SERS spectra extracted from the arrow-indicated points in the maps were baseline corrected and kept to scale for relative comparison and translated for better visualisaton. The spectrum marked with * was measured for the colloidal solution of antiCD19-PEG-NB-GNU.

Table 3.1 Band position and tentative band assignment for spectra extracted from the scans discussed above, by source: Raman reporter and cellular environment. Bands marked with * were integrated for creating the maps shown in Figure 3.2.

	Band position (cm^{-1})	Band assignment
NB	1360, 1641	other ring stretching vibrations
	665	in-plane CCC and NCC deformations
	595*	phenoxazine ring stretching vibration
Cellular components	1655	Amide I
	1450*	protein and lipid CH$_2$ and CH$_3$ deformation bands
	1330-1230	Amide III
	1003	phenylalanine ring breathing

3.1.3 Fluorescence Lifetime Imaging

FLIM has the ability to differentiate between the fluorescence lifetime of the cellular constituents, of approximately 4 ns, and that of the metal nanoparticles [16,17], where direct transitions between conduction band electrons and *d*-band holes result in lifetime values of less than 100 ps. This allows for a clear visualization of the particles inside the target cells (Figure 3.3B), while the optical sectioning that is possible due to the two-photon excitation reinforces the intracellular localization.
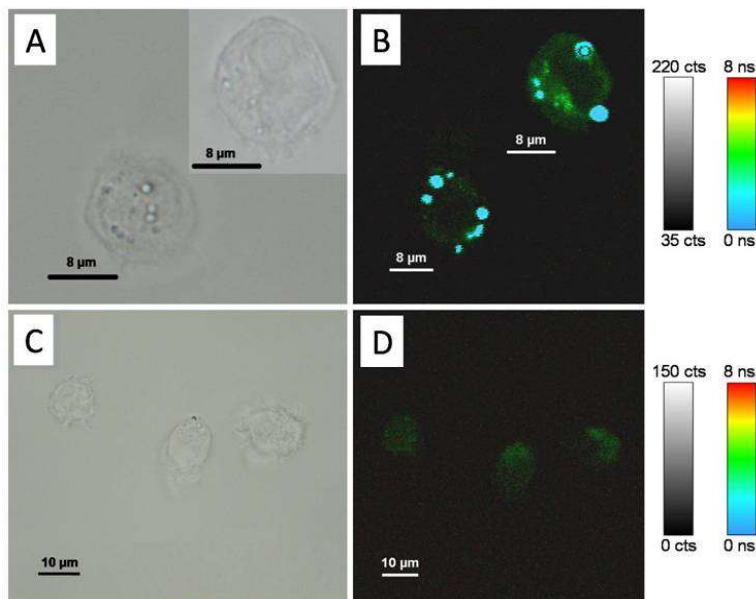

Figure 3.3 Bright-field optical images and TPE-FLIM images of CCRF-SB cells incubated with antiCD19-PEG-NB-GNU (A, B), and untreated cells (C, D).

3.2 Intracellular tracking of Hollow Nanospheres

3.2.1 Dark-Field microscopy

AntiCD19-PEG-NB-HNS are excellent candidates for dark-field imaging (Figure 3.4). This set of images was obtained by incubation of the cells with antiCD19-PEG-NB-HNS for different periods of time before fixation, and a time dependent trend is clearly observed: in the first 2 hours the particles are located mostly bound at the extracellular side of the plasmalemma (B, C), then internalization of a large number of nanoparticles occurs in the peripheral region of the cytoplasm (D, E), while after 24 hours (F) the particles are seen throughout the cell volume.
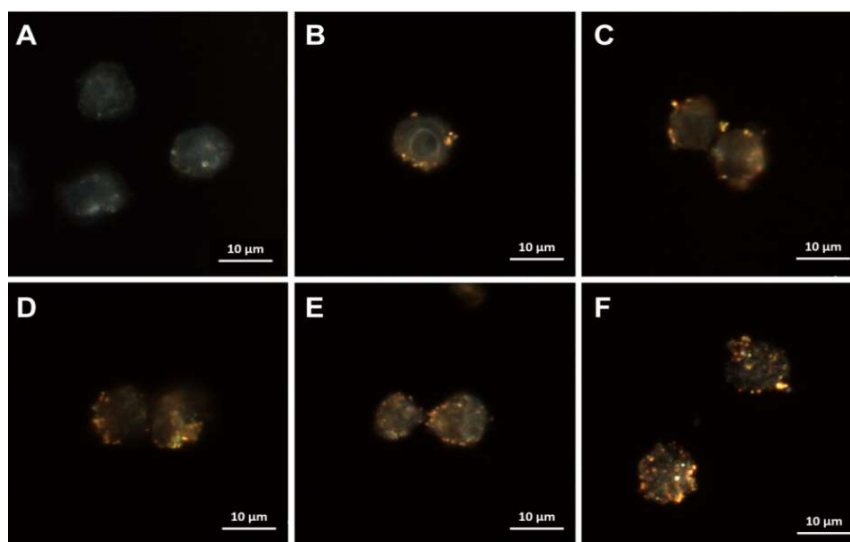
Figure 3.4 Dark-field images of SKW6.4 cells without nanoparticles (A), and incubated with antiCD19-PEG-NB-HNS for 30 min (B), 2 h (C), 6 h (D), 14 h (E) and 24 h (F).

3.2.2 Confocal Raman microscopy

Mapping of the uptake and distribution of antiCD19-PEG-NB-HNS inside target cells was done using two laser lines. Although the spectra of the particles measured in colloidal form at both excitations present quite a good signal of the reporter molecules at 595 cm^{-1} (*), it can be observed that SERS mapping based on the NB signal was not possible with the 785 nm laser excitation (Figure 3.5), but only with the 633 nm laser (Figure 3.6). At this wavelength, the laser line overlaps with the absorption spectrum of NB leading to a supplementary enhancement characteristic to Surface Enhanced Resonant Raman Scattering (SERRS) [18]. In this way, the 595 cm^{-1} signal of NB (cyan) is detectable and can be located in the same space where the SERS activity of the particles enhances the 1450 cm^{-1} organic signal (red) by 6 times compared to that in the control cells. Tentative assignments for cellular bands are summarized in Table 3.2 [19].

Table 3.2 Cellular specific band positions and tentative band assignments extracted from the scans discussed above.

Band position (cm^{-1})	Band assignment
1655	Amide I
1450	protein and lipid CH$_2$ and CH$_3$ deformation bands
1330-1230	Amide III
1126, 1094	phosphate symmetric and antisymmetric stretches of DNA backbone
1003	phenylalanine ring breathing
785	pyrimidine ring breathing and phosphodiester-stretch of DNA molecules

Figure 3.5 Bright-field optical images (A, C) and spectral maps of control untreated SKW6.4 cells (B) and antiCD19-PEG-NB-HNS treated cells (D), based on organic signal intensity (red) and NB signal (cyan), measured with **785 nm** excitation laser line. (E): Raman and SERS spectra extracted from the maps are baseline corrected, kept to scale for relative comparison, translated for better visualisaton. The spectrum marked with * was measured for the colloidal solution of antiCD19-PEG-NB-HNS.
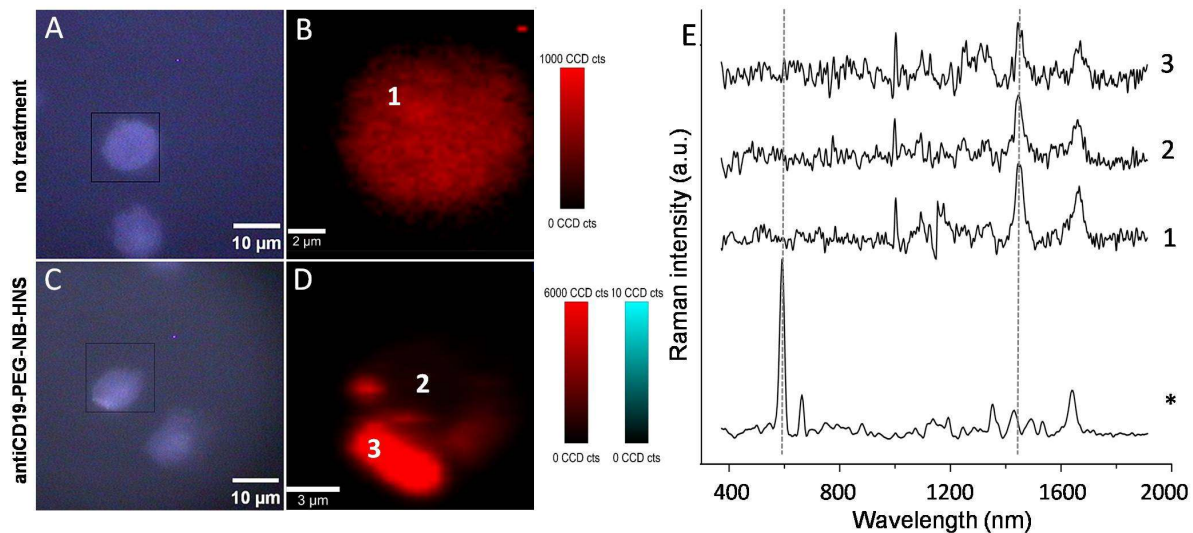

Figure 3.6 Bright-field optical images (A, C) and spectral maps of control untreated SKW6.4 cells (B) and antiCD19-PEG-NB-HNS treated cells (D), based on organic signal intensity (red) and NB signal (cyan), measured with **633 nm** excitation laser line. (E): Raman and SERS spectra extracted from the maps are baseline corrected, kept to scale for relative comparison, translated for better visualisaton. The spectrum marked with * was measured for the colloidal solution of antiCD19-PEG-NB-HNS.
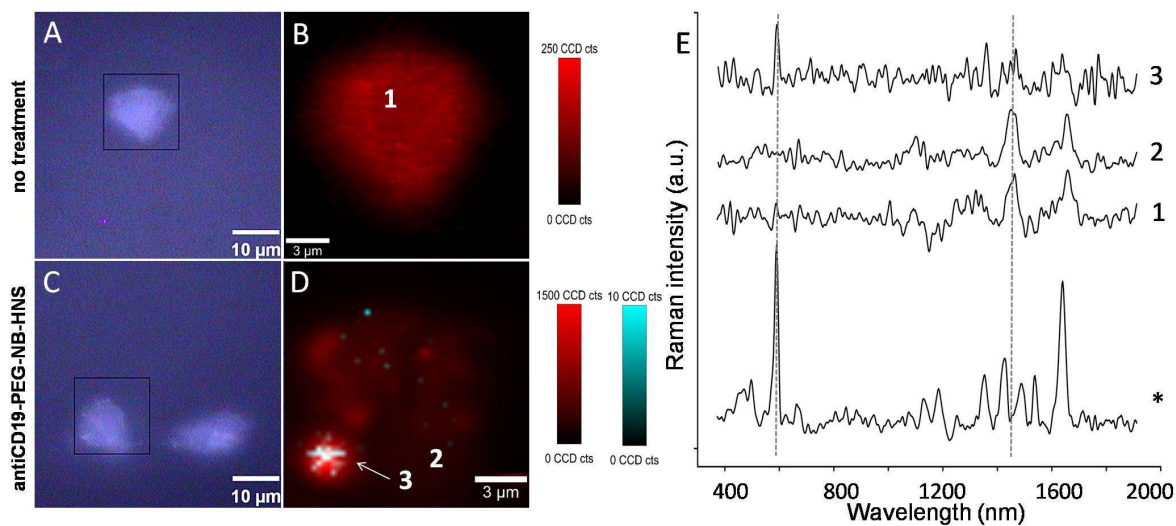
17

3.2.3 Fluorescence Lifetime Imaging

FLIM images and the corresponding corresponding bright-field optical images of nanoparticle-incubated and control cells are seen in Figure 3.7. Control cells have a weak signal with a lifetime of approximately 4 ns, while the incubated antiCD19-PEG-NB-HNS are differentiated with a lifetime shorter than 100 ps.
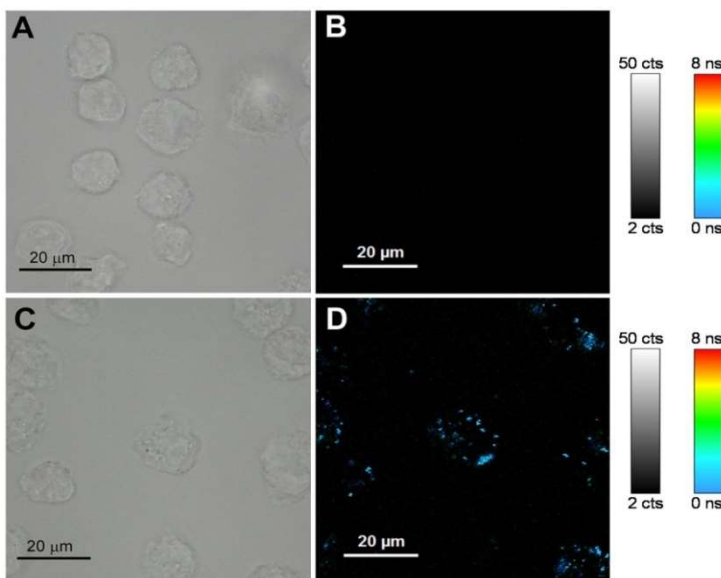

Figure 3.7 Bright-field optical images and TPE-FLIM images of untreated SKW6.4 cells (A, B), and incubated with antiCD19-PEG-NB-HNS (C, D)

4. TEM validation of antibody-based cell targeting by nanoparticles

4.1 Specificity of interaction of Gold Nanourchins

A high number of antiCD19-PEG-NB-GNU is observed at the intracellular level after the incubation with the target cells (Figure 4.1A, B), in contrast to the competitive binding assay data set, where a previous incubation with an excess of free antiCD19 molecules lead to binding and occupying of the CD19 molecules, leading to almost no interaction of the cells with the particles (C, D). Non-conjugated nanoparticles are for the most part not internalized, with very few exceptions of particles located in the cytoplasm or interacting with the extracellular side of the plasmalemma (E, F). The CD19-negative OCI-AML3 leukemia control cells, having no CD19 molecules on the surface, do not internalize CD19 targeted particles (G, H). These tests, as positive and negative control experiments demonstrate the specificity of the targeted nanourchins towards CD19-positive leukemic cells, and infer an internalization process based on receptor-

mediated endocytosis, demonstrated by the competitive binding assay, most probably *via* a clathrin-dependent internalization pathway, as CD19 was previously shown to be an internalizing epitope [20,21]. Moreover, none of the cellular samples show any abnormalities in regard to structural features as compared to the untreated cells (I, J).

4.2 Specificity of interaction of Hollow Nanospheres

The antiCD19-PEG-NB-HNS were found in important amounts either packed in endocytosis vesicles located in the proximity of plasma membrane, dispersed within the peripheral region of the cytosol of the target cells or tightly attached at the cell surface, especially on the cell extensions (Figure 4.2A, B). Pre-treatment with free antiCD19 molecules completely halted particle internalisation and reduced the contact to only a few particles attached on the cell extensions (C, D). Non-conjugated PEG-NB-HNS are almost never seen internalized, but the rare exceptions are single particles, located deeply in the cell volume, close to the nucleus (E, F, arrows). Only a small percentage of the CD19-negative cells were found to contain particles, and in those cases, in a significantly lower number compared to the CD19-positive cell line. The particles are either tightly packed in endo-lysosomal compartments resulted most likely from a nonspecific endocytosis (G, H), or they are localised in the cytosol as rare, single particles, probably internalised non-specifically, similarly to the non-conjugated PEG-NB-HNS discussed above. Cells incubated without nanoparticles displayed a normal ultrastructure, which was also maintained for those incubated with nanoparticles (I, J).

5. Therapeutic effect of antibody-targeted Nanourchins

5.1 Cellular toxicity of the particles, assessed by cell counting

Cell counting experiments were performed by counting the live cells in each well over a period of time and expressing cell viability as percentage of the control sample. The results show that the half maximal inhibitory concentration (IC_{50}) of antiCD19-PEG-NB-GNU is attained for a particle-bound antibody concentration as low as 0.17 ng/µl (correspondent particle concentration of 0.5×10^{-12} M) after the 5th day of incubation, while the same concentration brings the cell viability below the 25% level at the 7th day (Figure 5.1A). In contrast, for the free antiCD19 mAb to decrease cell viability below 50% after 7 days, concentrations above 0.42 ng/µl are needed (B). Therefore, it seems that a synergistic effect occurs when the antibody is
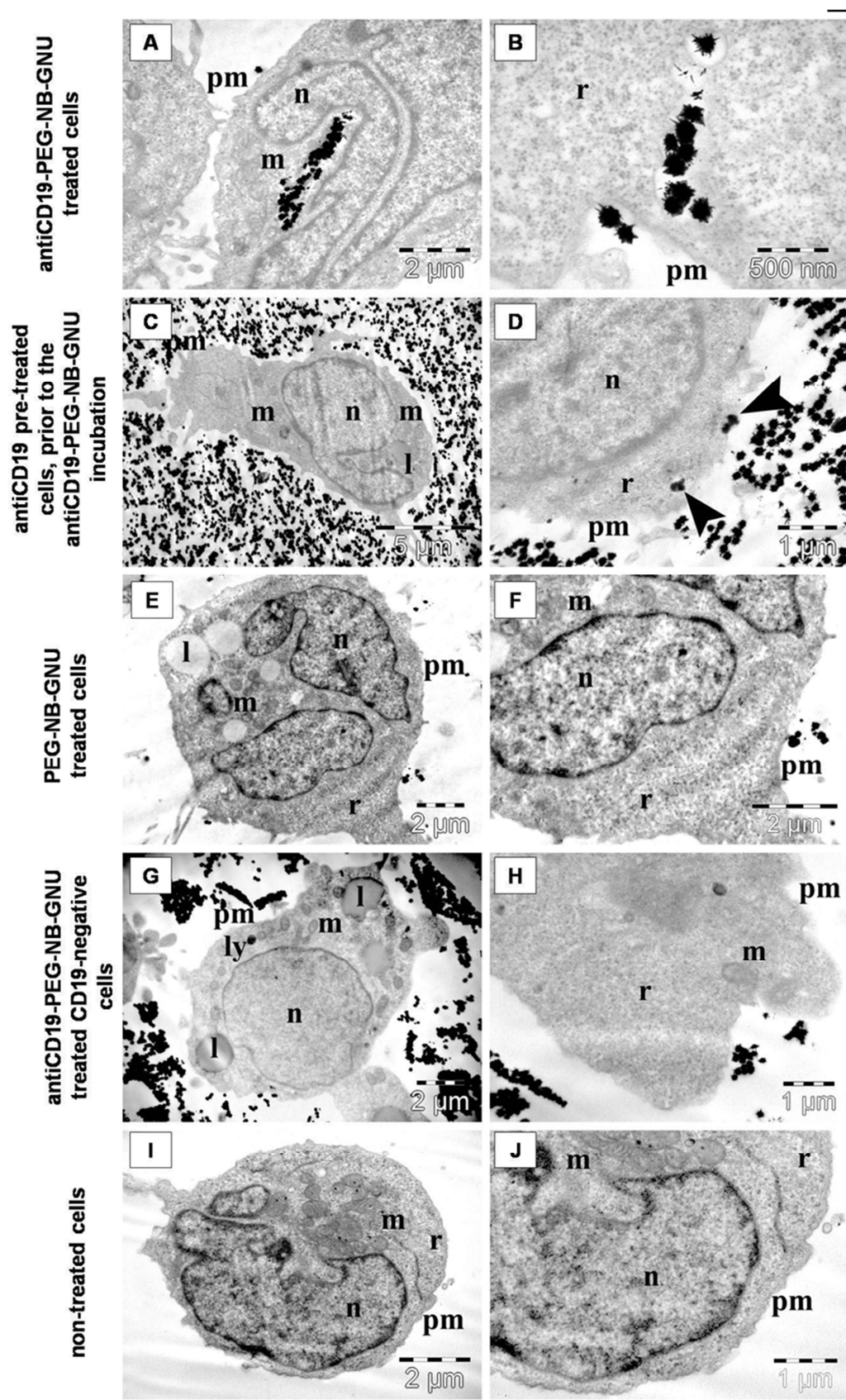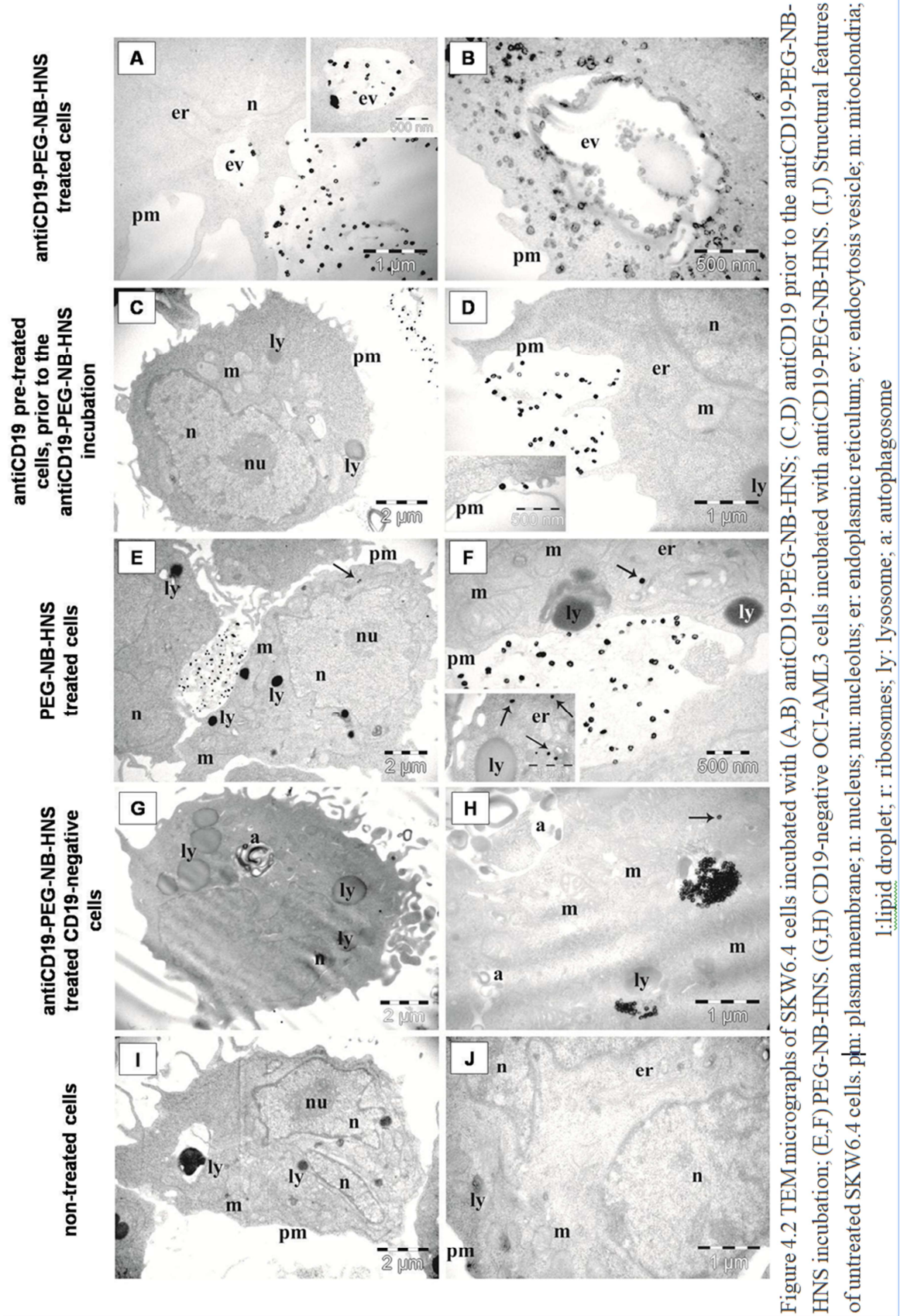
Figure 4.1 TEM micrographs of CCRF-SB cells incubated with (A,B) antiCD19-PEG-NB-GNU; (C,D) antiCD19 prior to the antiCD19-PEG-NB-GNU incubation; (E,F) PEG-NB-GNU. (G,H) CD19-negative OCI-AML3 cells incubated with antiCD19-PEG-NB-GNU. (I,J) structural features of untreated CCRF-SB cells. pm: plasma membrane; n: nuclei; m: mitochondria; l: lipid droplet; r: ribosomes; ly: lysosome.

20

Figure 4.2 TEM micrographs of SKW6.4 cells incubated with (A,B) antiCD19-PEG-NB-HNS; (C,D) antiCD19 prior to the antiCD19-PEG-NB-HNS incubation; (E,F) PEG-NB-HNS. (G,H) CD19-negative OCI-AML3 cells incubated with antiCD19-PEG-NB-HNS. (I,J) Structural features of untreated SKW6.4 cells. pm: plasma membrane; n: nucleus; nu: nucleolus; er: endoplasmic reticulum; ev: endocytosis vesicle; m: mitochondria; l: lipid droplet; r: ribosomes; ly: lysosome; a: autophagosome

21

conjugated onto the particles. Also, the free antibody molecules are protected from digestion when they are conjugated in the antiCD19-PEG-NB-GNU structure, since they maintain the correlation between concentration and effect for a longer time. The non-targeted PEG-NB-GNU sample (C) lacks the correlation between concentration and effect, and leads to cellular toxicity only above 1.23×10^{-12} M, after 7 days of incubation.
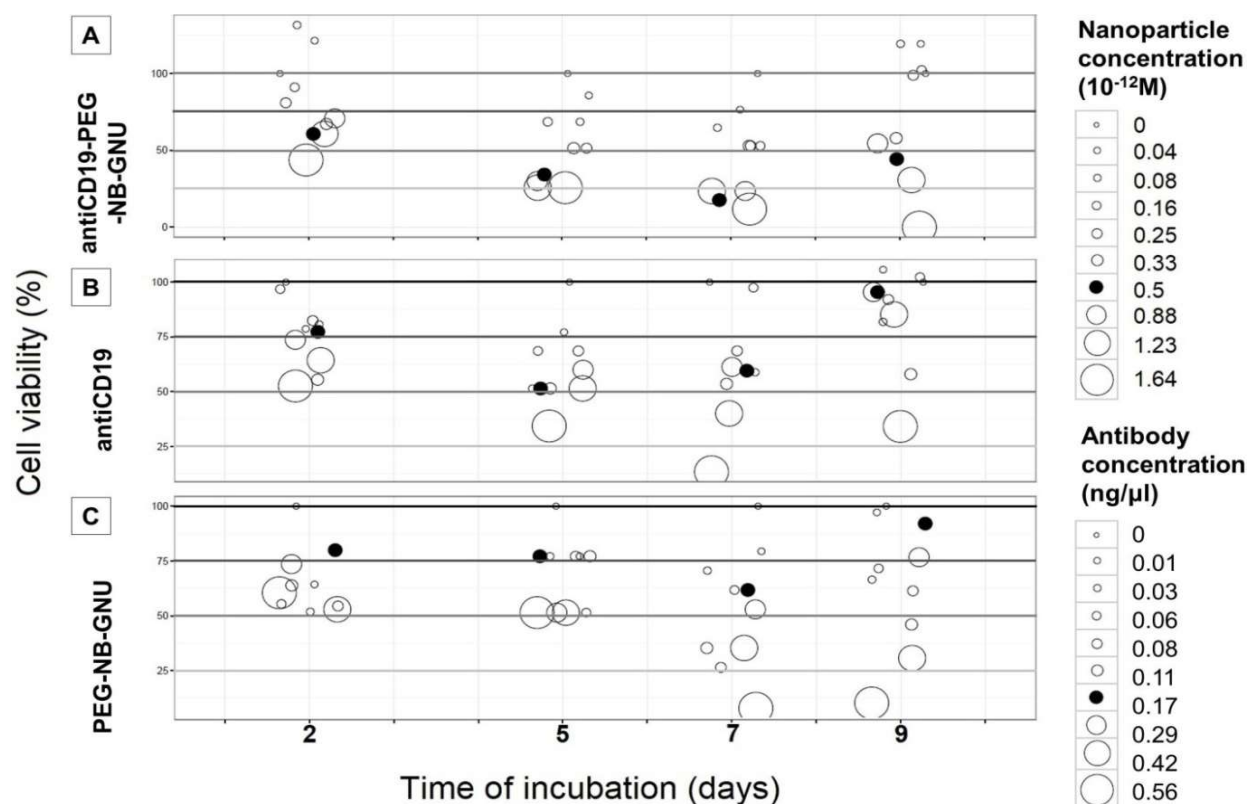

Figure 5.1 Cellular viability calculated after 2, 5, 7, 9 days of incubation with (A) antiCD19-PEG-NB-GNU; (B) free antiCD19 mAb; (C) PEG-NB-GNU. 100% represents the viability of control untreated sample. The diameter of the bubbles indicates the treatment concentration.

5 2 Cell cycle analysis by flow cytometry

The results show that after 24 hours of incubation with antiCD19-PEG-NB-GNU, cell cycle distribution differs from a normal pattern towards one with a decrease in the S phase and increases in the G phases (Figure 5.2A, black bars), which was shown to precede the induction of apoptosis [22]. Non-targeted particles induce similar cell-cycle deregulations but in a lower extent (dark grey bars), as conjugation of the antibodies onto the nanoparticle leads to an improved effect. By contrast, free mAb treatment leads to blocking of the cells in the S phase, probably

through more complex signaling pathways (light grey bars). As these measurements performed at 24 hours after incubation show some cellular toxicity of the particles, and the cell counting results show significant loss of cell viability after multiple days, we can infer that the mechanism of toxicity could be the induction of a delayed form of cellular death, known as late apoptosis, or post-mitotic apoptosis [23].
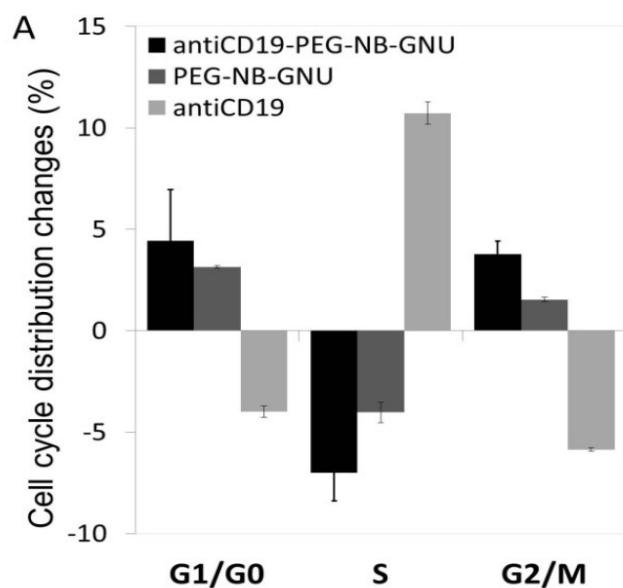

Figure 5.2 Variations in the CCRF-SB cell cycle distribution values (%) between the control non-treated sample and the treated samples, after 24 hours of incubation. Error bars are calculated based on triplicate data.

5.3 Metabolic activity and oxidative stress evaluation by MTS assay

The results indicate that MTS tetrazolium salt reduction in the CCRF-SB lymphoblasts increases with the increase in treatment dosage (Figure 5.3). Contrary to the cell counting and flow cytometry data, these results tend to raise the question of whether the particles are indeed toxic to the targeted cells, as the level of MTS reduction in the MTS assay is usually employed as a measure of cell viability. The notion that metabolic tetrazolium based assays are not suitable for cell proliferation measurements, especially in malignant and/or high cell density conditions was previously discussed [24], and the strict correlation with the NAD(P)H dehydrogenase activity was challenged. It was shown that the superoxide free radical ($O_2^-\bullet$) is a major reducing agent of the tetrazolium salts [25]. Thus, high oxidative stress in the cells, such as that produced by the presence of nanoparticles or certain drugs can lead to false-positive results based on $O_2^-\bullet$ concentrations [25]. This test is a valuable proof to an additional mechanism by which the antiCD19-PEG-NB-GNU induce their cytotoxic effect, namely a high oxidative stress due to the accumulation of the superoxide free radical, which precedes the induction of apoptosis [26].
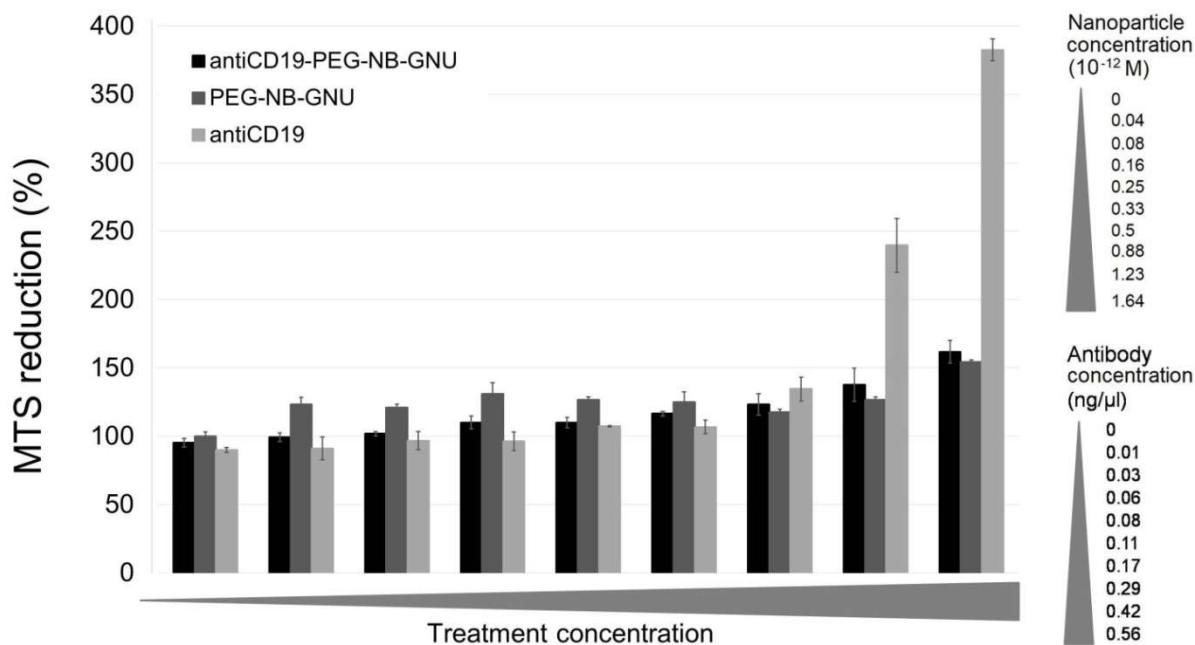
Figure 5.3 MTS reduction by CCRF-SB cells after 24 hours of incubation with a range of concentrations of antiCD19-PEG-NB-GNU, PEG-NB-GNU, and free antiCD19, relative to untreated control sample. Error bars are based on triplicate data.

6. Final conclusions

This work adds to the highly researched area of nanoparticle based theranostic approaches against malignant diseases, exploring particle morphologies, combined with a promising cellular marker that is recently booming as a target for B-cell leukemia treatments.

Hematological malignancies, as all cancers, should be identified as early in their onset as possible, to increase the patients' survival chances. The imaging potential showed here can be a valuable advancement in this medical direction, in combination with the therapeutic effect, thus employing the developed antiCD19-PEG-NB-GNU as theranostic agents.

● First, we showed the production of two types of NIR-responsive plasmonic nanoparticles, from synthesis tailoring to Raman tagging, polymer bio-compatibilisation and bio-marker targeting.

Gold nanourchins are produced through a controlled anisotropic growth reliant on Ag⁻ ions that tent to bind certain crystallographic facets on the gold particles.

The hollow nanospheres are created through the galvanic replacement method, where the sacrificial silver seed is displaced by gold atoms based on the difference in electrochemical potential between the two.

Raman tagging efficiency was assessed for multiple reporters and the most promising was chosen for further experiments.

Polymer cloaking was performed to avoid bio-fouling, offer steric stability and also structural stability. Additionally, functional groups on the outer side of the polymer offer a convenient site for further antibody conjugation.

The antibody chosen for specifically targeting a variety of B-cell leukemias was covalently attached to the nano-system.

● Second, the multimodal imaging potential of the particles was delineated for multiple imaging techniques, based on the physical properties of the noble-metal plasmonic nanoparticles used as the core elements in this work.

Dark-field imaging based on the high light scattering abilities of both particle types allows tracking of their presence in the cytosol or on the cellular extensions.

Through SERS imaging, the gold nanourchins are visualized inside target cells, by excitation with a NIR laser line. The Raman reporter was spectrally detected in points coinciding with the particle presence, where they also induced an organic signal increase due to the surface enhancement.

For the cells incubated with hollow nanospheres, SERRS signal was obtained with the 633 nm red laser line. This lower excitation wavelength coincides with the reporter absorption maximum, leading to a resonant interaction that explains the additional enhancement.

Both plasmonic nanoparticle types can be visualized inside the cells through the modern, non-invasive and fast Fluorescence-Lifetime Imaging technique, based in their short lifetime values (less than 100 ps), in contrast to the fluorescence lifetime of the cellular constituents (of approximately 4 ns).

● Then, the efficiency of the antibody to target cancer cells and the analysis of the interactions between the particles and the cells were demonstrated *via* TEM with a set of control samples.

Both nanourchins and hollow nanospheres are efficiently and specifically internalized by the targeted antigen-bearing cells. Competitive binding assays clearly proved the antibody-antigen binding, and the non-specific interaction with non-target cells was also excluded.

● Next, the therapeutic efficiency of the gold nanourchins was demonstrated against a B-cell leukemia cell line, and more tests brought information onto how the particles induce their effect.

> Direct cellular counting experiments performed over an extended period identified an antibody-conjugated particle concentration that can reduce cancer cell viability below 50% after 5 days of incubation and below 20% after one week.

> Flow cytometry experiments showed a blockage of the particle-treated cells in the G_1 and G_2 Growth phases after 24 hours, a circumstance that is known to precede the induction of apoptosis. Although some cellular damage is already noticeable, cell counting results begin to show stronger effect only after more time and are extended throughout more days, indicating towards a delayed-onset type of apoptosis as the cytotoxicity mechanism.

> The MTS assay shows a correlation between the increases in particle concentration and MTS reduction, which drives us to the conclusion that high oxidative stress levels are induced by the nanoparticles, and hints toward an additional front of cellular toxicity, that of oxidative stress.

● All in all, through this work we tried to contribute with a step forward in the fight against Acute Lymphoblastic Leukemia, by developing higly specific NIR responsive plasmonic nanoparticles with multiple imaging capabilities and potent therapeutic effects.

References

1.   Siegel, R. L., Miller, K. D. & Jemal, A. Cancer statistics. *CA. Cancer J. Clin.* **65**, 5–29 (2015).
2.   Pui, C.-H., Mullighan, C. G., Evans, W. E. & Relling, M. V. Pediatric acute lymphoblastic leukemia: where are we going and how do we get there? *Blood* **120**, 1165–1174 (2012).
3.   Loghavi, S., Kutok, J. L. & Jorgensen, J. L. B-Acute Lymphoblastic Leukemia/Lymphoblastic Lymphoma. *Am. J. Clin. Pathol.* **144**, 393–410 (2015).
4.   Basha, R., Sabnis, N., Heym, K., Bowman, W. P. & Lacko, A. G. Targeted Nanoparticles for Pediatric Leukemia Therapy. *Front. Oncol.* **4**, (2014).
5.   Arruebo, M. *et al.* Antibody-Conjugated Nanoparticles for Biomedical Applications, Antibody-Conjugated Nanoparticles for Biomedical Applications. *J. Nanomater. J. Nanomater.* **2009** (2009).
6.   Simon, T. *et al.* Design of FLT3 Inhibitor - Gold Nanoparticle Conjugates as Potential Therapeutic Agents for the Treatment of Acute Myeloid Leukemia. *Nanoscale Res. Lett.* **10**, 1–10 (2015).
7.   Yeh, Y.-C., Creran, B. & Rotello, V. M. Gold nanoparticles: preparation, properties, and applications in bionanotechnology. *Nanoscale* **4**, 1871–1880 (2012).
8.   Pellegrino, T. *et al.* On the Development of Colloidal Nanoparticles towards Multifunctional Structures and their Possible Use for Biological Applications. *Small* **1**, 48–63 (2005).

9. Ruoslahti, E., Bhatia, S. N. & Sailor, M. J. Targeting of drugs and nanoparticles to tumors. *J. Cell Biol.* **188**, 759–768 (2010).

10. Pernodet, N. *et al.* Adverse Effects of Citrate/Gold Nanoparticles on Human Dermal Fibroblasts. *Small* **2**, 766–773 (2006).

11. Jia, H. Y. *et al.* Potential Oxidative Stress of Gold Nanoparticles by Induced-NO Releasing in Serum. *J. Am. Chem. Soc.* **131**, 40–41 (2009).

12. Khlebtsov, N. & Dykman, L. Biodistribution and toxicity of engineered gold nanoparticles: a review of in vitro and in vivo studies. *Chem Soc Rev* **40**, 1647–1671 (2011).

13. Yuan, H. *et al.* Gold nanostars: surfactant-free synthesis, 3D modelling, and two-photon photoluminescence imaging. *Nanotechnology* **23**, 075102 (2012).

14. Nagy-Simon, T. *et al.* Antibody conjugated, Raman tagged hollow gold-silver nanospheres for specific targeting and multimodal Dark Field/ SERS/ Two Photon-FLIM imaging of CD19(+) B lymphoblasts. *ACS Appl. Mater. Interfaces* (2017). doi:10.1021/acsami.7b05145

15. De Gelder, J., De Gussem, K., Vandenabeele, P. & Moens, L. Reference database of Raman spectra of biological molecules. *J. Raman Spectrosc.* **38**, 1133–1147 (2007).

16. Zhang, Y., Yu, J., Birch, D. J. S. & Chen, Y. Gold nanorods for applications in biological imaging. in (eds. Achilefu, S. & Raghavachari, R.) 79101H (2011). doi:10.1117/12.877156

17. Zhang, Y., Yu, J., Birch, D. J. S. & Chen, Y. Gold nanorods for fluorescence lifetime imaging in biology. *J. Biomed. Opt.* **15**, 020504-020504–3 (2010).

18. McNay, G., Eustace, D., Smith, W. E., Faulds, K. & Graham, D. Surface-Enhanced Raman Scattering (SERS) and Surface-Enhanced Resonance Raman Scattering (SERRS): A Review of Applications. *Appl. Spectrosc.* **65**, 825–837 (2011).

19. Camp Jr, C. H. *et al.* High-speed coherent Raman fingerprint imaging of biological tissues. *Nat. Photonics* **8**, 627–634 (2014).

20. Krishnan, V. *et al.* CD19-Targeted Nanodelivery of Doxorubicin Enhances Therapeutic Efficacy in B-Cell Acute Lymphoblastic Leukemia. *Mol. Pharm.* **12**, 2101–2111 (2015).

21. Sapra, P. & Allen, T. M. Internalizing antibodies are necessary for improved therapeutic efficacy of antibody-targeted liposomal drugs. *Cancer Res.* **62**, 7190–7194 (2002).

22. Bernardi, A. *et al.* The antiproliferative effect of indomethacin-loaded lipid-core nanocapsules in glioma cells is mediated by cell cycle regulation, differentiation, and the inhibition of survival pathways. *Int. J. Nanomedicine* **8**, 711–729 (2013).

23. Halicka, H. D. *et al.* Cell cycle specificity of apoptosis during treatment of leukaemias. *Apoptosis Int. J. Program. Cell Death* **2**, 25–39 (1997).

24. Ng, K. W., Leong, D. T. W. & Hutmacher, D. W. The challenge to measure cell proliferation in two and three dimensions. *Tissue Eng.* **11**, 182–191 (2005).

25. Wang, S., Yu, H. & Wickliffe, J. K. Limitation of the MTT and XTT assays for measuring cell viability due to superoxide formation induced by nano-scale TiO2. *Toxicol. Vitro Int. J. Publ. Assoc. BIBRA* **25**, 2147–2151 (2011).

26. Kannan,& Jain, Oxidative stress and apoptosis. *Pathophysiol. Off. J. Int. Soc. Pathophysiol.* **7**, 153–163 (2000).

Result dissemination

- ***Papers***

i. **Tatar AS**, Nagy-Simon T, Tomuleasa C, Boca S, Astilean S, Nanomedicine approaches in acute lymphoblastic leukemia, *J. Controlled Release* 238; 123-138 (2016), IF = 7.877. AIS = 1.825.

ii. Nagy-Simon T, **Tatar AS**, Craciun AM, Vulpoi A, Jurj MA, Florea A, Tomuleasa C, Berindan-Neagoe I, Astilean S, Boca S, Antibody Conjugated, Raman Tagged Hollow

Gold−Silver Nanospheres for Specific Targeting and Multimodal Dark-Field/SERS/Two Photon-FLIM Imaging of CD19(+) B Lymphoblasts, *ACS Appl. Mater. Interfaces* 9(25), 21155-21168 (2017), IF = 8.097, AIS = 1.634

iii. **Tatar AS**, Jurj A, Tomuleasa C, Florea A, Berindan-Neagoe I, Cialla-May D, Popp J, Astilean S, Boca S, CD19-targeted, Raman tagged Gold Nanourchins as theranostic agents against Acute Lymphoblastic Leukemia (submitted to Colloids and Surfaces B: Biointerfaces)

- *Conference participations – oral presentations*

i. Nagy-Simon T, <u>**Tatar AS**</u>, Craciun AM, Vulpoi A, Jurj MA, Florea A, Tomuleasa C, Berindan-Neagoe I, Astilean S, Boca S, Hollow Gold-Silver Nanospheres for Specific Targeting and Multimodal Imaging of CD19(+) B Lymphoblasts, *European Conference on the Spectroscopy of Biological Molecules (ECSBM),* September 2017, Amsterdam, Netherlands

ii. <u>**Tatar AS**</u> , Jurj MA, Nagy-Simon T, Craciun AM, Berindan-Neagoe I, Florea A, Cialla-May D, Astilean S, Boca S, Novel theranostic agents against Acute Lymphoblastic Leukemia: CD19-targeting Gold Nanourchins, *2nd International Conference and Exhibition on Nanomedicine and Drug Delivery*, May 2018, Tokyo, Japan

- *Conference participations – posters*

i. <u>**Tatar AS**</u> , Nagy-Simon T, Boca S, Astilean S, Fabrication and conjugation of Au nanostars with Raman reporters for application in imaging and detection by SERS, *Raman4Clinics Summer School*, May 2016, Jena, Germany

ii. <u>Boca S</u>, **Tatar AS**, Nagy-Simon T, Tomuleasa C, Astilean S, Spectroscopic active, antibody conjugated gold nanoparticles for acute lymphoblastic leukemia detection and treatment, *SPIE Optics + Photonics*, August 2016, San Diego, California, SUA

iii. <u>**Tatar AS**</u> , Nagy-Simon T, Jurj MA, Berindan-Neagoe I, Tomuleasa C, Cialla-May D, Astilean S, Boca S, Anti-CD19 Gold Nanostars as New Therapeutic Vectors for the Treatment of Acute Lymphoblastic Leukemia, *2nd World Congress on Recent Advances in Nanotechnology (RAN'17), 2nd International Conference on Nanomedicine, Drug Delivery, and Tissue Engineering (NDDTE'17),* April 2017, Barcelona, Spain

iv. <u>**Tatar AS**</u> , Nagy-Simon T, Craciun A-M, Jurj MA, Berindan-Neagoe I, Astilean S, Boca S, Specific detection and imaging of Acute Lymphoblastic Leukemia cells using multimodal Gold Nanourchins, *FIRST COST ACTION CA17140 Training School, University of Trieste,* April 2019, Trieste, Italy.